

# An Efficient Integrated Two-Color Source for Heralded Single Photons

S. Krapick, H. Herrmann, V. Quiring, B. Brecht, H. Suche  
and Ch. Silberhorn

University of Paderborn, Department of Physics, Integrated Quantum Optics  
Group, Warburger Str. 100, 33098 Paderborn, Germany

E-mail: krapick@mail.upb.de

**Abstract.** We report on an integrated source for heralded single photons at telecom wavelengths based on a type-I two-color PDC process inside a Titanium-indiffused periodically poled Lithium Niobate waveguide. The on-chip integration of a passive symmetric wavelength division demultiplexer allows for spatial separation of signal and idler photons of more than 96.5 % in the respective output port. Our measurements of the heralded single photon states prove a preparation efficiency as high as 60 % and coincidences-to-accidentals ratios of up to 7400. For the low power regime we obtain a conditioned second order autocorrelation function as low as  $g^{(2)}(0) = 0.0038$  indicating almost pure photon pair generation. Moreover, the high brightness of our source was concluded from the large average photon number per pulse of  $\langle n_{\text{pulse}} \rangle = 0.24$  at power levels below  $100 \mu\text{W}$ .

PACS numbers: 03.67.Hk, 42.50.Dv, 42.65.Lm, 42.65.Wi, 42.79.Sz, 42.82.Bq,  
42.82.Cr, 42.82.Et

## 1. Introduction

Recent progress in the field of quantum information processing has highlighted the prospects of using integrated optic devices for quantum applications [1, 2, 3, 4, 5]. Integrated quantum photonics offers several advantages in comparison to free-space experimental setups with bulk optic components [6]. The miniaturization of systems with increased complexity does not only drastically reduce the required space and paves the way for future commercialization, but it also enables the implementation of optical networks with a large number of optical modes and extremely high stability.

In 2008 Politi and co-workers [7] have demonstrated the first quantum interference and photonic gates on-chip, while different groups have developed sophisticated and integrated experiments with two-photon interference [8, 9] or photon-entanglement [10, 11], controlled qubit-operations [12] as well as controlled phase shifts in linear optical circuits [5, 13]. In this year Metcalf et al have realized the first three-photon experiment inside a linear optical network [14].

However, in all of these experiments the preparation of the photon pairs has actually been performed outside the integrated devices employing traditional bulk crystal parametric down-conversion sources. The efficient coupling between these sources and the integrated circuit remains one bottleneck for designing systems with increasing complexity.

On the other hand remarkable efforts have been devoted to the development of integrated PDC sources for photon pair generation inside channel waveguides [15, 16, 17, 18, 19, 20, 21, 22] over the last decades. The main benefits of guided-wave PDC processes include high conversion efficiencies and spatial mode control.

Several techniques of waveguide fabrication in nonlinear materials have been developed to utilize parametric down-conversion sources, most of which concentrate on Lithium Niobate (LN) [23, 24, 25] and Potassium Titanyl Phosphate (KTP) [16, 26]. Among them, Titanium-indiffusion is a standard technique to manufacture waveguides in Lithium Niobate (Ti:LN) with extremely low loss [27] and the opportunity to guide light of both polarizations.

In this paper we report on an integrated type-I PDC source in Titanium-indiffused periodically poled Z-cut Lithium Niobate waveguides (Ti:PPLN) for photon pair generation. To allow for long-distance and low-loss fiber transmission of prepared PDC states within the telecom L-band around 1580 nm on the one hand and to apply Si-based heralding around 800 nm on the other hand, we focussed on non-degenerate PDC processes. An efficient integrated directional coupler provides us with on-chip spatial separation of the generated photons for simplified integration into larger networks and heralding experiments.

## 2. Device design, characterization method and technology

Our PDC source basically consists of two integrated building blocks, the physics of which will be explained in the following subsections. Figure 1 shows the general design of the device. In the periodically poled area (first building block) the PDC process takes place and the integrated S-bend type wavelength division demultiplexer (WDM coupler, second building block) allows for the subsequent spatial separation of signal and idler photons. Home-deposited high quality optical endface coatings provide our PDC source with low coupling losses of the respective colors.

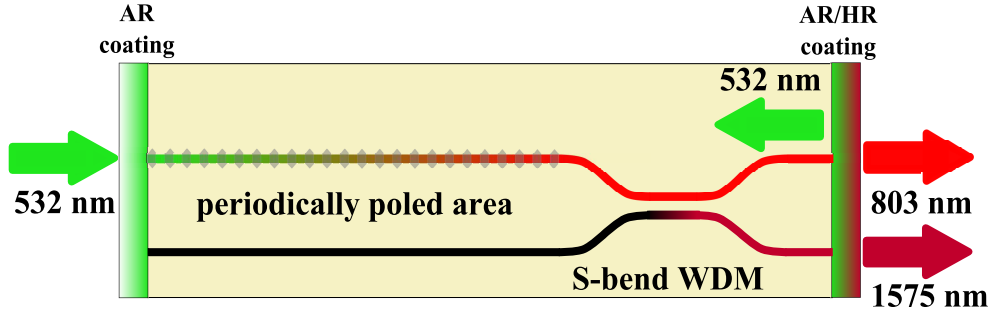


Figure 1: Schematic of the Ti:PPLN photon pair source

### 2.1. First building block - PDC process

In  $\chi^{(2)}$ -nonlinear optical materials, parametric down-conversion represents a three-wave-mixing process, where one pump photon (p) decays into two daughter photons, commonly labeled signal (s) and idler (i) with the signal photon having the higher angular frequency. For this process, the conservation of photon energy

$$\hbar\omega_p = \hbar\omega_s + \hbar\omega_i \quad (1)$$

must be fulfilled, where  $\omega = \frac{2\pi \cdot c}{\lambda} n$  describes the angular frequency of the photons and  $\lambda$  are their wavelengths, respectively. Likewise momentum conservation

$$\vec{k}_p = \vec{k}_s + \vec{k}_i \quad (2)$$

with  $\vec{k}$  representing the coresponding wave vectors defines the required phasematching condition. For bulk crystals collinear PDC processes are typically limited to only few wavelength combinations determined by tuning the angle of the crystal with respect to the propagation direction of the pump light.

In waveguides - due to the local increase of the refractive index - incoupled light can be confined to high intensities over comparably long distances by internal total reflection at the waveguide boundaries. This, in turn, causes the loss of the spatial degree of freedom in (2) and the wave vectors can be replaced by scalars of effective wave numbers for the individual guided mode

$$k(\lambda) = \frac{2\pi}{\lambda} n_{\text{eff}}(\lambda), \quad (3)$$

where  $\lambda$  again is the wavelength and  $n_{\text{eff}}(\lambda)$  represents the effective refractive index.

Usually, the co-directional travelling of the involved photons leads to a phase-mismatch  $\Delta k$  with

$$\Delta k = k(\lambda_p) - k(\lambda_s) - k(\lambda_i), \quad (4)$$

which has to be compensated for in order to achieve high conversion efficiencies.

Ferroelectric  $\chi^{(2)}$ -materials are characterized by their spontaneous polarization direction, which impacts their nonlinear susceptibility. By periodically inverting the spontaneous polarization we can introduce  $\pi$  phase shifts after odd integers of half the coherence length of a nonlinear process, yielding so-called quasi-phasematching. This is determined by the compensative element

$$\Delta k = \frac{m \cdot 2\pi}{\Lambda_G} = k_{\text{QPM}}, \quad (5)$$

where  $m$  is an odd integer, denoting the order of the phasematching, and  $\Lambda_G$  is the period of the inverted domains. Therefore conservation of momentum can be rewritten as

$$\Delta k = k_p - k_s - k_i - k_{\text{QPM}} = 0. \quad (6)$$

The periodic domain inversion provides us with length-dependent monotonically increasing intensities of signal and idler. The technological process to achieve periodic poling will be explained in section 2.4.

Together with the energy conservation, the quasi-phasematching allows for arbitrary wavelength combinations, simply by designing the appropriate poling periods. However, short pump wavelengths in combination with the degree of non-degeneracy of signal and idler lead to small poling periods required for the PDC process. As a technological limit for conventional poling techniques we can say that periods smaller than  $3 \mu\text{m}$  in LN are hard to fabricate homogeneously over large areas.

On the other hand, given a fixed poling period and pump wavelength, the wavelength combination of signal and idler is determined. Wavelength tuning is then possible only thermally due to the temperature dependence of the effective refractive indices.

Here we focus on PDC, in which pump photons with 532 nm wavelength - "seeing" only the extraordinary refractive index of the material - decay into signal and idler photons of the same polarization. This type-I PDC process accesses the highest nonlinear tensor element in Lithium Niobate  $d_{33}$  for a high conversion efficiency. Within our non-degenerate PDC processes, signal photons at 803 nm can be detected efficiently by Silicon avalanche photodiodes, while the idler photons have a wavelength of 1575 nm suitable for long-distance fiber transmission in the L-band. In order to determine the degree of non-degeneracy we varied the poling period of the device between 6.71 and 6.91  $\mu\text{m}$  in 0.02  $\mu\text{m}$  steps in several on-chip test structures.

## 2.2. *Heralding and conditioned $g^{(2)}(0)$*

In our experiments we pump our PDC source with pulsed light. For low pump powers one pair of photons is generated with a probability much lower than unity and higher photon number contributions are insignificant. Increasing pump power yields higher pair generation rates, however, higher photon number contributions cannot be avoided and are enlarged at the same time. While reliable heralding of single photons is only possible, if only one pair is generated, appearing higher order photon number contributions should be at least carefully quantified.

In 1977 Kimble et al [28] demonstrated photon anti-bunching effects within their characterization of light emitted by sodium atoms. For practical applications, a well established way to estimate the mean photon number statistics of a PDC source is the measurement of the anti-correlation parameter  $\alpha$ . In 1986 Grangier et al [29] applied the concept of Clauser [30] in a Hanbury Brown-Twiss geometry [31] to characterize anti-correlation phenomena by conditioned preparation of photon states. They introduced  $\alpha < 1$  to fulfill the nonclassicality criterion of the photon statistics. A quantitative determination of the anticorrelation parameter relates the count rates of binary photon detectors [32] within conditioned correlation measurements.

In our setup we use a free-running Silicon APD for the detection of signal photons at wavelengths around 800 nm, the detection of which electronically triggers the two other detectors to collect the conjugate telecom photons at around 1580 nm. Note

that in the following the term *trigger* is equal to the expressions *signal photons* and *heralding photons*. The schematic of our conditioned detection is shown in figure 2 (left).

The Si-APD detects with a detection rate  $R_{\text{Si,T}}$  and an efficiency  $\eta_{\text{det,Si}}$ . The other two detectors are InGaAs APDs and give "click"-rates of the collected idler photons  $R_{\text{InGaAs,i1}}$  and  $R_{\text{InGaAs,i2}}$ . These rates individually correspond to a two-fold coincidence of the trigger and the respective heralded photon. The input ports of the two InGaAs-APDs are assumed to be connected to a fiber-beamsplitter of 50/50 splitting ratio. Due to the property of a single photon being indivisible at a beamsplitter, a coincidence of "click"-events at both binary InGaAs-detectors can only happen, if there are at least two photons in front of the beamsplitter. Therefore the three-fold coincidence rate  $R_c$ , measuring the coincidences of all three detectors, directly represents the higher order photon contributions. The anti-correlation parameter  $\alpha$  for this case can be written as [29, 32]

$$\alpha = \frac{R_{\text{Si,T}} \cdot R_c}{R_{\text{InGaAs,i1}} \cdot R_{\text{InGaAs,i2}}}. \quad (7)$$

For the same kind of experimental setup, a similar expression for higher order photon contributions, which determines the purity of the single photon character of our PDC source, is known in the literature as the second-order auto-correlation or Glauber function  $g^{(2)}(0)$ . It was shown for example in [33], that

$$g^{(2)}(0) = \frac{p_c}{p_{\text{InGaAs,i1}} \cdot p_{\text{InGaAs,i2}}} \simeq 2 \frac{P(2)}{P(1)^2} \quad (8)$$

holds under the assumptions, that  $P(2) \ll P(1)$  and that we can neglect dark counts and use InGaAs-APDs with equal detection efficiencies  $\eta_{\text{det,InGaAs1}} = \eta_{\text{det,InGaAs2}} = \eta_{\text{det,InGaAs}}$ . In (8)  $p_{\text{InGaAs,i1}}$  and  $p_{\text{InGaAs,i2}}$  are the probabilities of an idler photon to be detected at the respective InGaAs-APDs, given a number of trigger events per unit time  $R_{\text{Si,T}}$ . The term  $p_c$  describes the probability of simultaneous detection events in both InGaAs-APD being triggered by the Silicon APD detection event.  $P(1)$  represents the probability of a prepared single photon state in front of a perfect 50/50 beamsplitter. Due to the indivisibility of photons,  $P(1)$  can be determined by summing up the individual click probabilities of both InGaAs-APDs. Then,  $P(1)$  is equal to the Klyshko efficiency[34] and given by

$$P(1) = \eta_K = p_{\text{InGaAs,i1}} + p_{\text{InGaAs,i2}} = \frac{R_{\text{InGaAs,i1}} + R_{\text{InGaAs,i2}}}{R_{\text{Si,T}}}. \quad (9)$$

Consequently, the individual click probabilities of identical InGaAs-APDs behind the perfect 50/50 beamsplitter can only be one half of the preparation probability  $P(1)$ . Hence we get

$$P(1) = 2 \frac{R_{\text{InGaAs,i1}}}{R_{\text{Si,T}}} = 2 \frac{R_{\text{InGaAs,i2}}}{R_{\text{Si,T}}}. \quad (10)$$

On the other hand,  $P(2)$  describes the probability of generated higher order photon states in front of an ideal beamsplitter, and it can be determined by measuring conditioned coincidences of both InGaAs-APDs behind the beamsplitter:

$$P(2) = 2 \frac{R_c}{R_{\text{Si,T}}} = 2 \cdot p_c. \quad (11)$$

Herein we assume, that the two-photon-pair states dominate the higher order photon contributions, i.e. we neglect states of  $n \geq 3$ . Note that the probability  $P(2)$  is a

factor of two larger than the probability  $p_c$ . This is due to the fact that a single two-photon contribution splits up with the probability of  $p_{\text{split}} = 0.5$ , whereas the probabilities of the two-photon contribution to arrive at the same beamsplitter output is  $p_{\text{out},1} = p_{\text{out},2} = 0.25$ .

Substituting (9) and (11) into (8) we get for the second order auto-correlation function

$$g^{(2)}(0) = 4 \frac{R_{\text{Si,T}} R_c}{(R_{\text{InGaAs},i1} + R_{\text{InGaAs},i2})^2}, \quad (12)$$

which the mean photon number  $\langle n \rangle$  is related to [35] via:

$$\langle n \rangle = \frac{1}{1 - g^{(2)}(0)}. \quad (13)$$

For  $\eta_{\text{det,InGaAs}} < 1$ , we can introduce a heralding efficiency  $\eta_H$  as a measure of the ratio of idler photons, which arrive at the InGaAs-APDs. In other words, the heralding efficiency represents how good the prepared PDC states are transferred through the optical path behind the source. This includes all kind of losses in any optical component, but excludes the InGaAs-detector efficiencies. The heralding efficiency can be written as

$$\eta_H = \frac{\eta_K}{\eta_{\text{det,InGaAs}}}. \quad (14)$$

A different aspect of performance and brightness of PDC sources is the so-called coincidences-to-accidentals ratio (CAR). As known for sources operating with a continuous wave pump, one may estimate the CAR, when shifting the time delay of the arrival of heralded and trigger photons with respect to each other. This ratio is given by the maximum rate of two-fold coincidences of trigger and InGaAs-APD divided by the rate of two-fold coincidences far away from temporal overlapping (e.g. 5 ns when using a 1.2 ns internal gating time  $\tau_{\text{gate}}$  of the InGaAs-detector):

$$CAR_{\text{cw}} = \frac{R_{\text{c,double}}(P_p, \Delta\tau = 0)}{R_{\text{c,double}}(P_p, \Delta\tau = T)}, \quad |T| \gg \tau_{\text{gate}}. \quad (15)$$

In contrast to that, in our pulsed experiment (see figure 2 (right)) we can define three different  $CAR$  to characterize the performance of our source. The first one is equivalent to the cw-case and indicates the gating properties, where the time difference  $T$  must not be the same as the time between two pump pulses. Therefore we label it  $CAR_{\Delta\tau} \hat{=} CAR_{\text{cw}}$ . This ratio can be interpreted as a measure of pump-induced fluorescence. It will have low values, if parasitic fluorescent processes with lifetimes much longer than the gate width are present and contribute to two-fold coincidences.

We expect higher order photon pair contributions in our PDC process, which have an impact on the two-fold coincidence rate and thus will increase the Klyshko efficiency at elevated pump power levels. Therefore we express  $CAR_{\Delta\tau}$  in a more suitable way for conditioned measurements using the definition of (15):

$$CAR_{\Delta\tau} = \frac{\eta_K(P_p, \Delta\tau = 0)}{\eta_K(P_p, \Delta\tau = T)}, \quad (16)$$

where  $|T|$  must be larger than the gating time window width but smaller than the repetition time  $\tau_{\text{rep}}$  of our pump.

In figure 2 (right) an expected typical temporal PDC behaviour is shown. From this we can define a second coincidence-to-accidentals ratio  $CAR_{\text{rep}}$  by measuring coincidences between generated trigger from pulse  $A$  and artificially time shifted idler

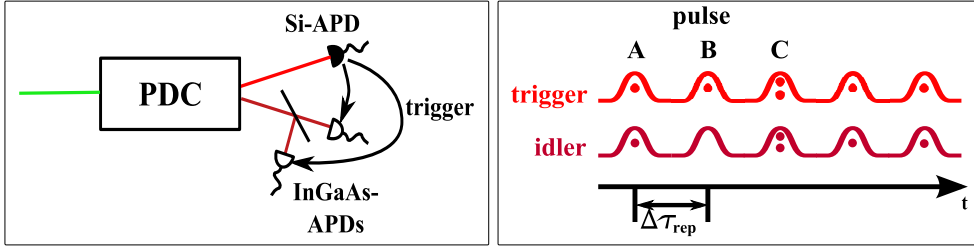


Figure 2: Conditioned PDC detection scheme (left); Temporal PDC event behaviour with pulsed pump (right)

photons of the neighbouring pulses  $B$  or  $C$ . At a given repetition rate the time of the artificial shift must be an integer multiple of the repetition time  $\tau_{\text{rep}}$ . We get for  $CAR_{\text{rep}}$ :

$$CAR_{\text{rep}} = \frac{R_{c,\text{double}}(P_p, \Delta\tau = 0)}{R_{c,\text{double}}(P_p, \Delta\tau = m \cdot \tau_{\text{rep}})}, \quad m \in \mathbb{N}. \quad (17)$$

In this definition we assume that the probability of heralding one photon in each pulse equals  $p$ . If an idler photon is present in a pulse  $B$  or  $C$  next to the heralding pulse, the probability of announcing this particular idler photon is equal to the photon pair generation probability, because the non-matched heralding event is actually not correlated. The coincidence counts will therefore grow linearly with increasing pump power, if deadtime effects or photon pairs of higher order play no major role. Besides that, at a given pump power, the value of  $CAR_{\text{rep}}$  must be the same for every neighbouring pulse  $B$ ,  $C$  etc. With this,  $CAR_{\text{rep}}$  indirectly is a measure of the generated photon number per pulse and thus for the brightness of the source.

Thirdly, if we call higher order photons (HOP) accidentals, we define a ratio  $CAR_{\text{HOP}}$ , which sets the maximum two-fold coincidence rate in relation to the rate of three-fold coincidences within the very same  $g^{(2)}(0)$  measurement. From this we have an indicator for the purity of heralded single photons:

$$CAR_{\text{HOP}} = \frac{R_{c,\text{double}}(P_p, \Delta\tau = 0)}{R_c(P_p, \Delta\tau = 0)}. \quad (18)$$

The latter two coincidences-to-accidentals ratios are expected to have their highest values at the lowest rate of pump photons, and they will decrease to 1 with increasing pump power.

### 2.3. Second building block - WDM coupler

In order to separate the generated signal and idler photons spatially, we implemented a WDM-coupler behind the periodically poled area. Figure 3 (left) shows a detailed geometry of our integrated WDM-coupler building block. The coupler was chosen to be an S-bend type to reduce bending losses [36] and phase jumps at the interconnections of the three building parts: input ports, stem length  $L_C$  and output ports.

The most accurate way to treat a waveguide directional coupler with finite channel separation is to describe its properties in terms of local normal modes of the dual channel structure [37, 38, 39]. In our case the local normal modes of the coupler with symmetric S-bends comprise of a symmetric (00) and an anti-symmetric (10) mode. As long as the channel separation is sufficiently large compared to the wavelength, the

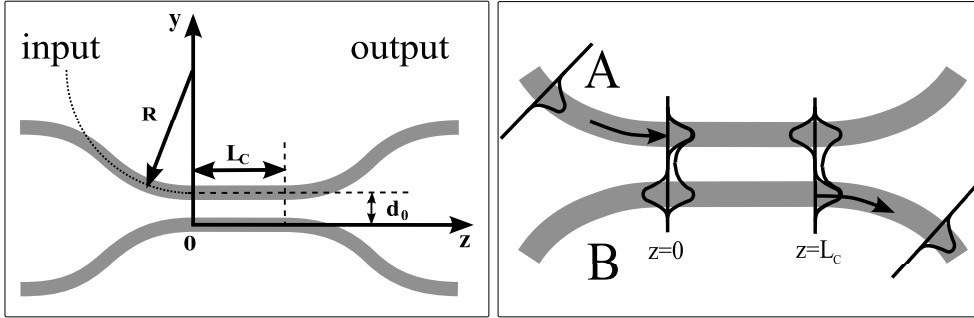


Figure 3: Details of the WDM coupler (left); Local normal mode evolution scheme (right)

propagation constants of the two modes are degenerate:  $\beta_{00}(d \gg \lambda) = \beta_{10}(d \gg \lambda)$ . The propagation constants are represented by

$$\beta_{i,j}(d(z), \lambda) = \frac{2\pi}{\lambda} n_{\text{eff},ij}(d(z), \lambda), \quad (19)$$

which depends on the respective wavelength and exponentially on the distance  $d(z)$ . For decreasing distances, the propagation constants of the symmetric and anti-symmetric mode split up. This provides us with wavelength selective coupling: There is only coupling for wavelengths for which the phase difference between the two modes changes upon propagation in z- direction:

$$\Delta\phi = \int_0^{z'} (\beta_{00}(d(z)) - \beta_{10}(d(z))) dz \neq 0. \quad (20)$$

The launching of light into one input channel is the result of constructive interference of these local normal modes in the launching channel and a destructive interference in the other channel. Upon approaching of the two channels towards the homogeneous central section of the coupler, the degeneracy of the propagation constants of the two modes is gradually removed. This causes an increasing amount of phase difference  $\Delta\phi$  and the corresponding interference change between the two modes. As a result the power flow gradually bounces from the launching channel to the adjacent one. Complete overcoupling to the new channel is achieved if the accumulated phase difference is  $\Delta\phi = \pi$ . For non-degenerate PDC we can design the coupler such that coupling is only provided for fundamental waveguide mode of the idler wavelength whereas the signal power almost fully remains in the launching channel.

In our source we arbitrarily have defined  $z = 0$  at the interface between the S-Bend input and stem length part. Input and output ports consist of arc elements and the channel separation  $d(z)$  for  $-R \leq z \leq 0$  and  $L_C \leq z \leq L_C + R$  can be described as

$$d(z) = d_0 + 2 \cdot R \left( 1 - \sqrt{1 - \left(\frac{z}{R}\right)^2} \right), \quad (21)$$

where  $R = 160$  mm is the radius of curvature - sufficiently large to prevent additional bending loss - and  $d_0$  is the (fixed) separation of the two parallel waveguides within the stem length section.



The maximum accumulated phase difference  $\Delta\phi_B$ , contributed by the input and output S-bend ports, consists of individual phases  $\phi_{\text{in}}$  and  $\phi_{\text{out}}$ , which are equal for symmetry reasons. We can write explicitly

$$\Delta\phi_B = \phi_{\text{in}} + \phi_{\text{out}} = 2 \int_{-R}^0 \beta_{00}(d(z)) - \beta_{10}(d(z)) dz, \quad (22)$$

where we justifiably assume that practically no coupling occurs in the regions  $z < -R$  and  $z > L_C + R$  because of the large separation of the waveguides. The straight stem length part contributes to the overall phase difference with

$$\Delta\phi_S = [\beta_{00}(d_0) - \beta_{10}(d_0)] L_C \stackrel{!}{=} \pi - \Delta\phi_B \quad (23)$$

for one full power transfer to the adjacent waveguide. In order to achieve higher order power transfer, the accumulated phase must be an integer of  $\Delta\phi_S = m \cdot \pi$ ,  $m \geq 2$ . With (23) we can estimate the stem length  $L_C$  for our test structures. Therefore we applied FEM calculations [39, 40] to determine the respective propagation parameters  $\beta_{i0}(d(z))$  with  $i \in \{0, 1\}$  very precisely.

In our source we only varied the coupler stem length from 2750 to 4250  $\mu\text{m}$  within different test structures to determine the optimum coupling behavior of the idler wavelength, which is shown schematically in figure 3 (right). We can also get information about the overall power transfer contribution from the S-bend ports by the extrapolation to  $L_C = 0$ . The coupling of the signal wavelength will not take place at the same time significantly, because of the strong confinement in its fundamental waveguide mode. As a measure for the separation, we define the splitting ratio or WDM efficiency for the respective wavelength

$$\eta_{\text{WDM},s/i} = \frac{P_X(L_C, \lambda_{s/i})}{P_X(L_C, \lambda_{s/i}) + P_B(L_C, \lambda_{s/i})} \quad (24)$$

Herein X denotes the adjacent (cross) arm and B is the index for the original (bar) arm.

In order to be able to address optical fibers embedded in Silicon V-groves, we have set the on-chip-separation of the output ports of the WDM coupler fix to 165  $\mu\text{m}$ .

#### 2.4. Waveguide, WDM and poling technology

The properties of Z-cut X-propagation Lithium Niobate prescribe us a well-defined procedure for the fabrication of Titanium-indiffused waveguides and periodic poling structures in order to get PDC sources of good quality, namely sources with low intrinsic loss and with high conversion efficiency.

In our case, Titanium of a well-defined and homogeneous thickness was deposited by electron beam evaporation onto the Z-surface of the 80 mm long and 0.5 mm thick sample. The waveguide structure was defined by photolithographic delineation of the Titanium layer using deep UV contact printing. These metal stripes were subsequently indiffused at 1060C for 8.5 hours, defining half-gaussian concentration profiles [40]. With the linear relationship between the Ti-concentration and the extraordinary refractive index increase, we accordingly yield a refractive index profile, which is half-gaussian as well. Note that in our case all waves taking part in the PDC process see the extraordinary refractive index. The idler wave can only be guided in its fundamental spatial mode, whereas pump and signal photons can couple to higher order modes due to dispersion of the refractive index change.

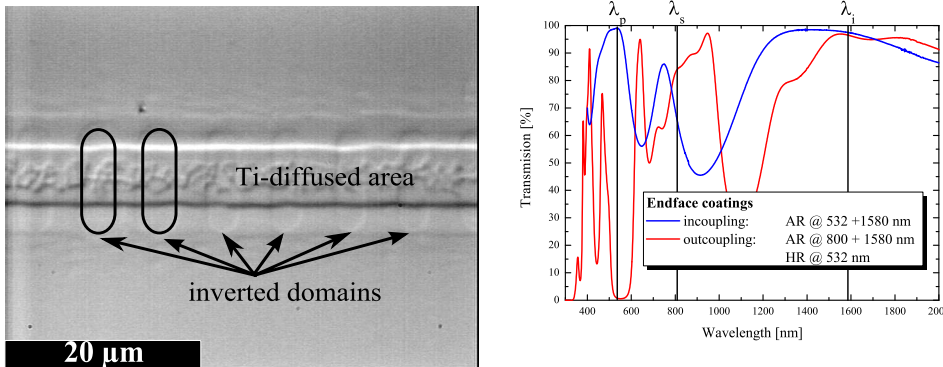


Figure 4: Domain structure of the periodically poled waveguide area (left); characteristics of the end-face coatings (right)

For periodic poling the standard electric field assisted poling method [41] was applied, using a waveguide selective segmented resist patterning for electrical insulation and Lithium Chloride solution as the contact electrolyte. By applying short voltage pulses of 11.5 kV and monitoring the displacement current due to the periodic polarization reversal the accumulated charge was controlled to provide the right duty cycle of the 30 mm long domain grating with around  $7\ \mu\text{m}$  poling period (see figure 4 (left)).

In order to achieve the best possible coupling of light into and out of the waveguides, the end-facettes were polished perpendicularly to the propagation direction and coated with dielectric layer stacks. Therefore, different end-face coatings (EFC) have been designed and deposited for an optimum incoupling of the pump as well as for the best possible outcoupling of signal and idler wavelengths including the reflection of the pump. The transmission characteristics for both coatings are shown in figure 4 (right). Note that the coating at the waveguide output reaches more than  $R_{\text{EFC},p} = 0.99$  of reflection for the pump, while it allows for the idler wavelength to be transmitted with more than  $T_{\text{EFC},i} = 0.965$ .

### 3. Experimental Setup

Figure 5 illustrates the experimental setup. It shows that the optical setup in principal can be separated into three major divisions: incoupling, sample adjustment and analysis part.

We used a frequency-doubled pump source (Katana-05, Onefive GmbH Zürich), which converts amplified diode laser light at 1064 nm to the green in a second harmonic generation process. In order to spectrally filter out any residual 1064 pump light we added a prism-based cleaning stage in front of a variable attenuator and neutral density filters, which allow for additional power control. The required TM polarization for the type-I PDC process was set with a  $\lambda/2$ -plate right in front of an AR-coated incoupling lens.

The sample adjustment part of the setup basically consists of a home-assembled high-precision 5-axis translation/rotation stage. The PDC source is stabilized at a

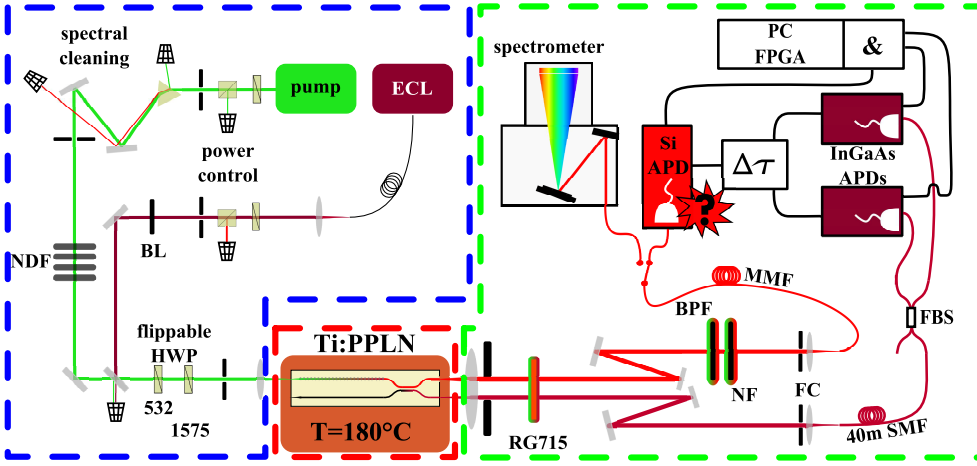


Figure 5: Experimental setup for spectral characterization and conditioned measurements; NDF: neutral density filters, BL: beam blocker, ECL: external cavity laser for idler coupling adjustment, HWP: half-wave plate, RG715: customized absorptive filter, NF: needle filter, BPF: band-pass filter, FC: fiber coupling stages, SMF: single mode fiber, MMF: multi-mode fiber, FBS: fiber beamsplitter 50/50,  $\Delta\tau$ : delay generator, APD: avalanche photodiode, FPGA: field programmable gate array

temperature sufficiently high to prevent photorefractive damage ( $T \geq 140^\circ\text{C}$ ). The operation point for our heralding experiments was set to  $T_{\text{OP}} = 185^\circ\text{C}$ .

The highest degree of experimental flexibility was achieved by keeping the analysis part of the setup in a free-space configuration as far as possible. An AR-coated outcoupling lens allows for the transmission of signal and idler beams by more than 97% while it magnifies the sample's intrinsic spatial separation of signal and idler.

Right behind the outcoupling lens we placed a home-deposited RG715 filter, which is transmissive for signal and idler at  $T_{\text{RG715},s/i} = 97\%$  each. The filter prevents the green pump light neither to be transmitted nor to cause fluorescence in the absorber significantly. This was realized by the deposition of a 16-layer AR/HR coating. The filter's overall pump suppression was measured with a spectrophotometer and is larger than six orders of magnitude.

Two D-shaped mirrors further split up the on-chip spatially separated beams to a signal and an idler arm. The signal arm consists of two additional spectral filters and a multimode fiber coupling stage, which is connected to a spectrometer system (Andor iKon-M 934P-DD/Shamrock SR-303iA) for spectral PDC characterization. It can also be connected to the free-running Silicon avalanche photo diode (Si-APD, Perkin Elmer SPCM-AQRH-13) for the heralding experiments and for conditioned  $g^{(2)}(0)$  measurements. The Si-APD is specified to have a detection efficiency of  $\eta_{\text{det,Si}}(\lambda_s) = 55\%$  at around 800 nm and was measured to have an average dark count rate of  $R_{\text{T,dark}} = (238 \pm 16) \text{s}^{-1}$ .

The idler arm also includes a high precision fiber coupling stage for injecting the idler photons to an InGaAs-APD (ID Quantique ID201) via 40 m of AR-coated single mode fiber, the length of which ensures the optical compensation of electrical delays. For  $g^{(2)}(0)$  measurements an additional fiber beam splitter was connected in between and enables us to address a second InGaAs-APD. At the idler wavelength both APDs

have specified detection efficiencies of  $\eta_{\text{det,InGaAs}}(\lambda_i) = 0.23$ . Their internal acquisition time gate for idler click events was set to 2.5 ns with zero additional deadtime.

Electronical compensation of the occurring temporal gap in the arrival of pair photons at the respective detector was realized using a Stanford Research DG645 delay generator. This device also compensates for the electronic delays of the heralding Si-APD and the internal delay of the InGaAs-APDs. Data acquisition and the evaluation of single and coincidence events were carried out with an FPGA interface card operating at 40 MHz - corresponding to data acquisition time bins of 25 ns length.

#### 4. Results and Discussion

Prior to the PDC characterization, linear properties of the device have been determined classically. As one bottleneck, which generally limits the heralding efficiency in fiber-based PDC detection devices, the mode size of the idler wave and its symmetry both are important for the overlap integral to spatial modes of single mode fibers (SMF), since any asymmetry decreases this overlap. Therefore we carefully analyzed the waveguide mode sizes. From the mode's half widths at half maximum we calculated 90.1% as the theoretical mode overlap integral to a standard single mode fiber mode and TM polarization. In contrast to this theoretical value, we only managed to couple in  $\eta_{\text{SMF}} = 79\%$  of the power at idler wavelength into the SMF, measuring the power of coherent radiation in front of the SMF coupling lens and at the output of the 40 m fiber. Together with the throughput of the applied fiber beam-splitter

$$T_{\text{FBS}} = \frac{P_{\text{out},1} + P_{\text{out},2}}{P_{\text{in}}} = 0.955,$$

the benchmark for the heralding efficiency is  $\eta_{\text{SMF},i} = 75.4\%$ , neither taking into account any additional loss from filters etc. in our setup nor from the PDC device itself (e.g. WDM, end-face coating).

A second important feature of the waveguides is its low intrinsic loss of 0.07 dB/cm in average, which we measured for straight control channels on the same chip. For this measurement we applied a low-finesse Fabry-Pérot-interferometric method [27].

We additionally determined the spatial separation of the signal and idler beams within our integrated WDM coupler behind the periodically poled area. Therefore we varied the WDM coupler stem length  $L_C$  in several test structures and applied two different measuring techniques. By launching coherent radiation at the idler wavelength into the WDM we measured the output powers in both arms. But for the signal wavelength - due to dispersion - we were not able to couple in laser light into the fundamental waveguide mode. We therefore directly accessed the generated PDC spectra, which were maximized for the fundamental mode combination, with a spectrometer system in both arms and calculated the respective splitting ratio from the power equivalent PDC peak count rates. As an alternative measure for the separation we also defined and calculated the power suppression

$$S_s = 10 \cdot \log \left( \frac{P_X(L_C, \lambda_s)}{P_B(L_C, \lambda_s)} \right) \quad (25)$$

and

$$S_i = 10 \cdot \log \left( \frac{P_B(L_C, \lambda_i)}{P_X(L_C, \lambda_i)} \right). \quad (26)$$

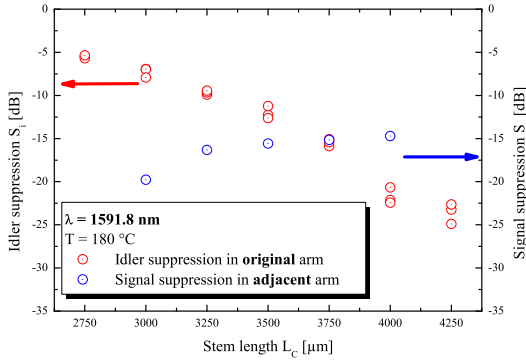


Figure 6: WDM coupler characteristics for signal (red) and idler (blue)

In (25) and (26) again the power index X denotes the cross arm, while B indicates the bar output arm. Remember, that the idler wavelength should couple to the adjacent (cross) arm, while the signal photons should remain in the original (bar) arm. The results of the suppression evaluation are shown in figure 6 for the respective wavelength. We see that the suppression clearly is dependent on the stem length of the WDM coupler. It is significant for the heralding efficiency that in the optimum case at  $4000 \mu\text{m}$  WDM coupler stem length, the signal power remains in the original arm with  $\eta_{\text{WDM},s} \geq 0.965$ , while the idler power is coupling to the adjacent arm with  $\eta_{\text{WDM},i} \geq 0.991$ . This corresponds to  $S_{s,\text{opt}} = -15 \text{ dB}$  and  $S_{i,\text{opt}} = -20.6 \text{ dB}$  suppression in the undesired arms, respectively.

Together with the maximum transmission of the end-face AR-coating for the idler wavelength, with the idler arm transmission of  $T_{\text{arm},i} = 91\%$  (outcoupling lens, mirrors and spectral filter) as well as with the fiber coupling efficiency and InGaAs-detector efficiency, we were limited to a maximum experimentally achievable Klyshko efficiency in our setup of

$$\eta_{\text{K},\text{exp}} = \eta_{\text{det,InGaAs}}(\lambda_i) \cdot \eta_{\text{SMF},i} \cdot T_{\text{arm},i} \cdot T_{\text{EFC},i} \cdot \eta_{\text{WDM},i} = 0.151$$

corresponding to a maximum heralding efficiency of  $\eta_{\text{H},\text{exp}} = 65.6\%$ . This upper experimental boundary only holds for very low pump power levels, where higher order photon pair contributions can be neglected.

Basic nonlinear characteristics of the PDC source have been determined by measuring the spectral behaviour, when changing the device's temperature or its poling period. Both dependencies are plotted as normalized curves in figure 7 and indicate the wavelength tunability to be either coarse (with poling period) or fine (with temperature). The latter result also determines the wavelength stability of the source. Note that there are practically no significant sidepeaks or higher order mode excitations indicating an excellent waveguide homogeneity and the best possible incoupling of the pump to its fundamental waveguide mode. In addition we can clearly identify a broad structure in the lower wavelength region next to the PDC signal peaks in figure 7 and figure 8. We suspect this to be nonlinear Čerenkov radiation associated with the quasi-phases-matching process [42].

In order to distinguish the PDC signal photons from unwanted spectral noise counts, we included a dielectric needle filter in the signal arm. With this, the spectral characteristics of the PDC source in the Silicon detection band exhibits noise that

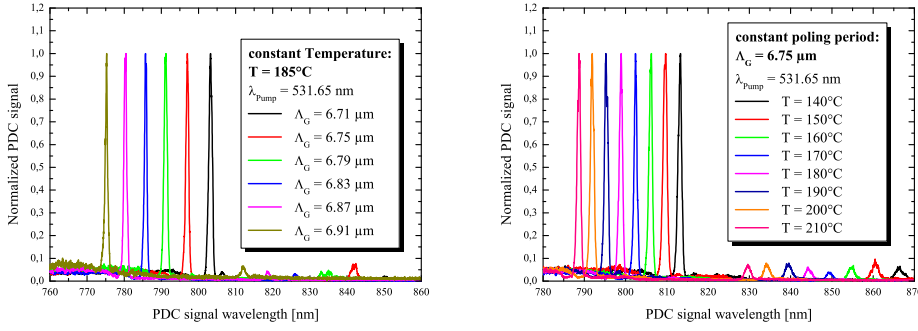


Figure 7: Tunability of the PDC signal wavelength with the crystal’s poling period (left) and the device’s temperature (right)

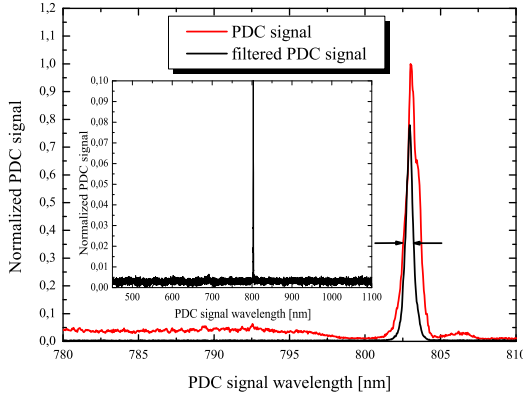


Figure 8: Unfiltered (red) and needle-filtered PDC signal (black), inset: background spectral characteristics

contributes less than 0.6% of the maximum PDC signal level. The needle filter has a FWHM bandwidth of 0.5 nm and a maximum classical transmission of  $T_{\text{NF},s} = 0.78$  as shown in figure 8 and its inset.

In power-dependent measurements we observed the rates of the trigger at 803 nm  $R_{\text{Si},T}$ , the two-fold coincidences  $R_{c,\text{double}} = R_{\text{InGaAs},i1} + R_{\text{InGaAs},i2}$  and the triple coincidences  $R_c$  within 1 s of measurement time. Repeating this measurement a 100-fold provides us with small error bars for the different rates, the three-fold coincidence rate of which contributes the highest uncertainties. Figure 9 shows the respective rates in double-logarithmic scaling. It can be seen that the trigger rate has an almost linear dependency on increasing pump power, while the coincidence rates both increase superlinear. The two-fold coincidence rate shows this behaviour above  $10 \mu\text{W}$ , whereas the triple-coincidences rate increases superlinearly at power levels lower than  $1 \mu\text{W}$ . Note that the linearity of the trigger rate disappears above  $10^5$  counts per second due to deadtime effects.

From the detected count rates we calculated the Klyshko efficiency and the heralding efficiency according to (9) and (14), which are plotted in figure 10 (left).

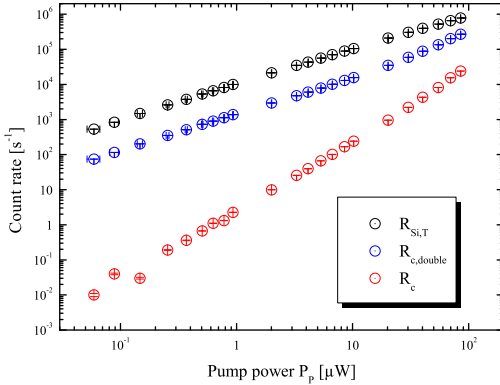


Figure 9: Pump-dependent count rates of the trigger (black), the sum of the two-fold coincidences (blue) and the triple coincidences (red) in conditioned measurements

The  $g^{(2)}(0)$  values and the anti-correlation parameter  $\alpha$  were calculated using (12) and (8), respectively.

Obviously an almost constant Klyshko efficiency for pump powers lower than  $10 \mu\text{W}$  can be concluded. This result indicates, that the influence of higher order photon pairs significantly sets in above this power level due to the increasing number of pump photons per pulse. Within the range up to  $10 \mu\text{W}$  both -  $R_{\text{Si,T}}$  and  $R_{\text{c,double}}$  - are depending almost linear on the pump power and result in constant heralding and Klyshko efficiencies.

In figure 10 (left) we identified a heralding efficiency of 60% at pump powers less than  $10 \mu\text{W}$ , where almost only first order photon pairs contribute to the measurement (compare plots in figure 9). To the best of our knowledge, this is the first time, that in a Ti:PPLN based type-I PDC source such high heralding efficiencies have been reported, while other sources of efficiently heralded single photons (see for example [43, 44, 45]) rely on bulk nonlinear materials or photonic crystal fibers. The fiber coupling limitations of our lab system, described in the upper part of this section, can be overcome, when we use a completely fiber-based setup in the future with spectral filters of the same loss characteristics like the free-space option. We think that this should further improve the heralding efficiencies to around 80%.

As shown in figure 10 (right), the auto-correlation function at very low power levels ( $P_p \leq 1 \mu\text{W}$ ) reaches a minimum value of  $g^{(2)}(0) = 0.0038$ , which could be driven even lower at the cost of the heralding rate. But for applications with this kind of PDC sources, low trigger rates are always related to low transmission rates, and a trade-off between high rates and purity of the single photons is unavoidable. In addition we can conclude, that the approximation made in (8) and in [33, 32] is valid and suitable for low pump powers. At the upper end of our power scale, we see that  $g^{(2)}(0)$  tends to be one, which would correspond to an infinite average photon number. Note that at these high pump power levels our assumption,  $P(2) \ll P(1)$ , is no longer valid. Additionally the triggering rate and the triple coincidence rate,  $R_{\text{Si,T}}$  and  $R_{\text{c}}$ , both tend to be overestimated due to higher order photon contributions. Especially the Si-APD fires only once, when there is more than a single trigger photon arriving. Furthermore, internal deadtime effects of the InGaAs-APDs limit the repetition rate of the detection of double coincidences. The general tendency of the  $g^{(2)}(0)$  to approach 1 at pump powers higher than  $30 \mu\text{W}$  can be seen in the graph. Therefrom we can

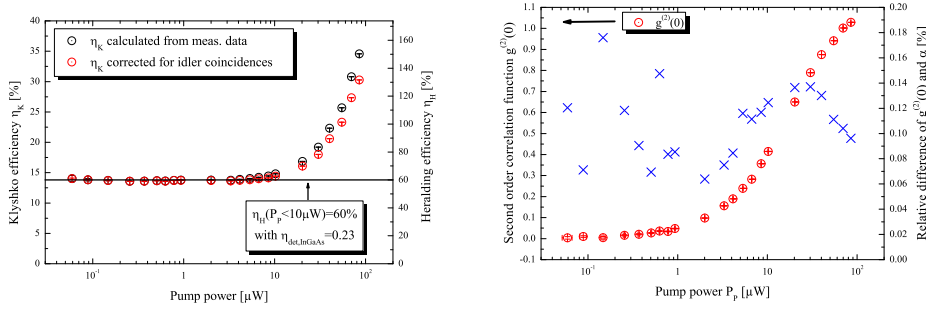


Figure 10: Pump-dependent Klyshko efficiency and heralding efficiency (left); auto-correlation function  $g^{(2)}(0)$  and its relative difference to the anti-correlation parameter  $\alpha$  (right)

conclude, that trigger rates higher than 310kHz should be avoided for this kind of detectors in combination with our kind of measurement. Figure 10 (right) also shows, that the relative differences between the calculated values of  $g^{(2)}(0)$  and the anti-correlation parameter  $\alpha$  are very small, so that we can conclude the equivalence of (7) and (12) for our measurements.

We additionally determined the source's heralding efficiency around the optimum time delay between trigger and heralded photons at two different power levels. For this we measured the count rates in temporal step widths of 0.2 ns for 5 s each. The characteristics in figure 11 show almost gaussian shape, being a meter of the intrinsic gate width of the InGaAs-APDs of  $\tau_{\text{gate}} = (1.16 \pm 0.32)$  ns. The error includes timing jitters of the InGaAs-APD, the Si-APD and of the delay generator. The overlapped view of both curves visualizes the increase of the Klyshko efficiency with increased pump power due to higher order photon pair contributions. It can also be derived from the data and from the inscriptions of figure 12, that the Klyshko efficiency is not affected by pump-induced fluorescence of any optical component, because the high  $CAR_{\Delta\tau}$  did not decrease significantly. In particular, at 500 nW and 5  $\mu$ W the coincidences-to-accidentals ratios were calculated to be 1383 and 1165, respectively. Please note, that in figure 11 this feature cannot to be seen intuitively due to the scaling of the accidentals.

In figure 12 we plotted all three coincidence-to-accidentals ratios. Even with its double-logarithmic scaling we can point out, that especially the  $CAR_{\text{rep}}$  for two adjacent pulses asymptotically tends to the value of 1 at the highest observed pump power, while the  $CAR_{\text{HOP}}$  dropped from 7440 to around 10 at the same power level. The latter result is an additional proof of the usefulness of a trade-off between high heralding rates and a low  $g^{(2)}(0)$ .

One of the most important benchmarks of our source is its brightness. Therefore we determined the pump dependent mean number of generated photons per pulse. The values, which we get from dividing the heralding rate  $R_{\text{Si,T}}$  by the transmissivities of all optical components in the signal arm and by the repetition rate  $R_{\text{rep}} = 10$  MHz, are shown in figure 13. We identified a linear dependency as expected. At the lowest pump power available in our set of data we got a mean photon number per pulse of  $\langle n_{\text{pulse,min}} \rangle = 2 \cdot 10^{-4}$ . At the highest applied pump power of 85.14  $\mu$ W we calculated



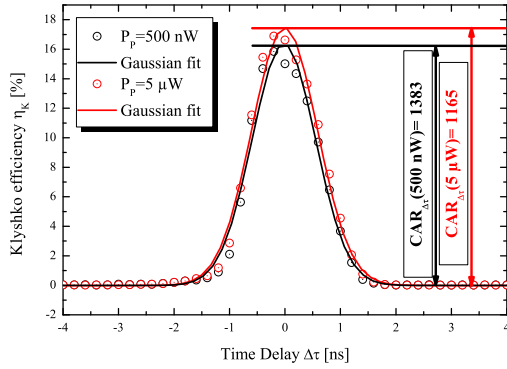


Figure 11: Dependency of the Klyshko efficiency on the temporal overlap between signal and idler detection

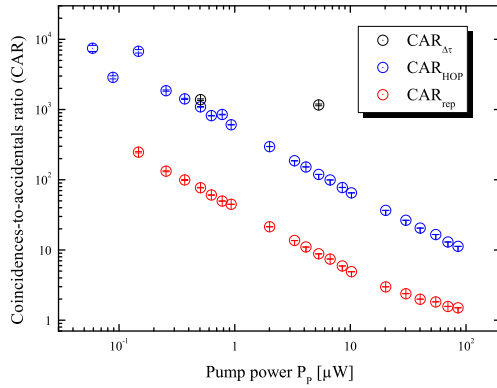


Figure 12: Pump dependency of the three calculated coincidence-to-accidentals ratios

the mean photon number per pulse to be  $\langle n_{\text{pulse,max}} \rangle = 0.24$ . From the slope of the graph in figure 13 we can extrapolate an average photon number per pulse of  $\langle n_{\text{pulse,th}} \rangle \approx 34$  at  $P_P = 10$  mW of cw-equivalent pump power, which is easily available with our pump laser.

## 5. Conclusion and outlook

We demonstrated the on-chip integration of a waveguide-based type-I PDC source in combination with a passive WDM coupler for the spatial separation of signal and idler beam. The source shows close-to-perfect demultiplexing behavior for wavelengths of 803 nm and 1575 nm as well as very low scattering loss. We managed to achieve heralding efficiencies of 60% and a second order correlation function as low as 0.0038. At pump power levels around  $10 \mu\text{W}$  the second order auto-correlation function still does not exceed  $g^{(2)}(0) = 0.42$ , which indicates a minor influence of higher order photon pairs to the detection. At higher power levels  $P_P \geq 30 \mu\text{W}$  the Si- and InGaAs-detectors tend to saturate, which distorts the calculation of correct  $g^{(2)}(0)$  values.

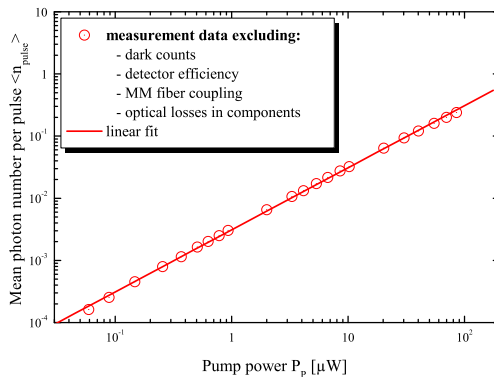


Figure 13: Generated mean photon number per pulse in dependency on the pump power

The high brightness of the source was derived from the extrapolation of the mean photon number per pulse of  $\langle n_{\text{pulse,th}} \rangle \approx 34$  at  $P_p = 10$  mW cw-equivalent pump power. We determined a coincidence-to-accidentals ratio of  $CAR_{\text{HOP}} > 7400$  at low power levels for the comparison of heralded single photons and higher order photon contributions.

Due to the strong dependence of the heralding efficiency on the coupling of the heralded photons to optical fibers, we will proceed in our work the implementation to an all-fiber-connected device. We think this will increase the heralding efficiency to around 80%.

## Acknowledgments

The authors want to thank R. Ricken for the helpful technology discussions. This work was funded by the European Union in the QuRep project (reference: 247743).

## References

- [1] S. Tanzilli, A. Martin, F. Kaiser, M.P. De Micheli, O. Alibart, and D.B. Ostrowsky. On the genesis and evolution of integrated quantum optics. *Laser & Photonics Reviews*, 6(1):115–143, 2012.
- [2] A. Martin, O. Alibart, M. P. De Micheli, D. B. Ostrowsky, and S. Tanzilli. A quantum relay chip based on telecommunication integrated optics technology. *New Journal of Physics*, 14(2):025002, 2012.
- [3] A. Christ and C. Silberhorn. Limits on the deterministic creation of pure single-photon states using parametric down-conversion. *Phys. Rev. A*, 85:023829, Feb 2012.
- [4] N. Sangouard, B. Sanguinetti, N. Curtz, N. Gisin, R. Thew, and H. Zbinden. Faithful entanglement swapping based on sum-frequency generation. *Phys. Rev. Lett.*, 106(12):120403, March 2011.
- [5] D. Bonneau, E. Engin, K. Ohira, N. Suzuki, H. Yoshida, N. Iizuka, M. Ezaki, C. M. Natarajan, M. G. Tanner, R. H. Hadfield, S. N. Dorenbos, V. Zwiller, J. L. O’Brien, and M. G. Thompson. Quantum interference and manipulation of entanglement in silicon wire waveguide quantum circuits. *New Journal of Physics*, 14(4):045003, 2012.
- [6] E. Pomarico, B. Sanguinetti, T. Guerreiro, R. Thew, and H. Zbinden. Mhz rate and efficient synchronous heralding of single photons at telecom wavelengths. *Opt. Express*, 20(21):23846–23855, Oct 2012.
- [7] A. Politi, M.J. Cryan, J. G. Rarity, S. Yu, and J. L. O’Brien. Silica-on-silicon waveguide quantum circuits. *Science*, 320:646, 2008.

- [8] G. D. Marshall, A. Politi, J. C. F. Matthews, P. Dekker, M. Ams, M. J. Withford, and J. L. O'Brien. Laser written waveguide photonic quantum circuits. *Opt. Express*, 17(15):12546–12554, Jul 2009.
- [9] A. Peruzzo, A. Laing, A. Politi, T. Rudolph, and J. L. O'Brien. Multimode quantum interference of photons in multiport integrated devices. *Nature Communications*, 2(224):224, March 2011.
- [10] J. C. F. Matthews, A. Politi, A. Stefanov, and J.L. O'Brien. Manipulation of multiphoton entanglement in waveguide quantum circuits. *Nature Photonics*, 3(6):346–350, June 2009.
- [11] P. Shadbolt, T. Vértesi, Y.-C. Liang, C. Branciard, N. Brunner, and J. L. O'Brien. Guaranteed violation of a bell inequality without aligned reference frames or calibrated devices. *Sci. Rep.*, 2:470, June 2012.
- [12] H.W. Li, S. Przeslak, A. O. Niskanen, J. C. F. Matthews, A. Politi, P. Shadbolt, A. Laing, M. Lobino, M. G. Thompson, and J. L. O'Brien. Reconfigurable controlled two-qubit operation on a quantum photonic chip. *New Journal of Physics*, 13(11):115009, 2011.
- [13] B. J. Smith, D. Kundys, N. Thomas-Peter, P. G. R. Smith, and I. A. Walmsley. Phase-controlled integrated photonic quantum circuits. *Opt. Express*, 17(16):13516–13525, Aug 2009.
- [14] B. J. Metcalf, N. Thomas-Peter, J. B. Spring, D. Kundys, M. A. Broome, P. Humphreys, X.-M. Jin, M. Barbieri, W. S. Kolthammer, J. C. Gates, B. J. Smith, N. K. Langford, P. G. R. Smith, and I. A. Walmsley. Multi-photon quantum interference in a multi-port integrated photonic device. *ArXiv e-prints*, 1208:4575, August 2012.
- [15] S. Tanzilli, H. De Riedmatten, H. Tittel, H. Zbinden, P. Baldi, M. De Micheli, D.B. Ostrowsky, and N.t Gisin. Highly efficient photon-pair source using periodically poled lithium niobate waveguide. *Electronics Letters*, 37(1):26–28, jan 2001.
- [16] K. Banaszek, A. B. U'Ren, and I. A. Walmsley. Generation of correlated photons in controlled spatial modes by downconversion in nonlinear waveguides. *Opt. Lett.*, 26(17):1367–1369, Sep 2001.
- [17] M. C. Booth, M. Atatüre, G. Di Giuseppe, B. E. A. Saleh, A. V. Sergienko, and M. C. Teich. Counterpropagating entangled photons from a waveguide with periodic nonlinearity. *Physical Review A*, 66(2):023815, 2002.
- [18] J. Chen, A. J. Pearlman, A. Ling, J. Fan, and A. L. Migdall. A versatile waveguide source of photon pairs for chip-scale quantum information processing. *Optics Express*, 17(8):6727–6740, April 2009.
- [19] D. Bonneau, M. Lobino, P. Jiang, C. M. Natarajan, M. G. Tanner, R. H. Hadfield, S. N. Dorenbos, V. Zwiller, M. G. Thompson, and J. L. O'Brien. Fast path and polarization manipulation of telecom wavelength single photons in lithium niobate waveguide devices. *Phys. Rev. Lett.*, 108:053601, Jan 2012.
- [20] F. Kaiser, A. Issautier, L. A. Ngah, O. Danila, H. Herrmann, W. Sohler, A. Martin, and S. Tanzilli. High-quality polarization entanglement state preparation and manipulation in standard telecommunication channels. *New Journal of Physics*, 14(8):085015, 2012.
- [21] M. Karpinski, C. Radzewicz, and K. Banaszek. Dispersion-based control of modal characteristics for parametric down-conversion in a multimode waveguide. *Opt. Lett.*, 37(5):878–880, Mar 2012.
- [22] A. S. Solntsev, A. A. Sukhorukov, D. N. Neshev, and Y. S. Kivshar. Spontaneous parametric down-conversion and quantum walks in arrays of quadratic nonlinear waveguides. *Physical Review Letters*, 108(2):023601, January 2012.
- [23] E. Pomarico, B. Sanguinetti, N. Gisin, R. Thew, H. Zbinden, G. Schreiber, A. Thomas, and W. Sohler. Waveguide-based opo source of entangled photon pairs. *New Journal of Physics*, 11(11):113042, 2009.
- [24] O. Alibart, D. B. Ostrowsky, P. Baldi, and S. Tanzilli. High-performance guided-wave asynchronous heralded single-photon source. *Opt. Lett.*, 30(12):1539–1541, Jun 2005.
- [25] A. Martin, A. Issautier, H. Herrmann, W. Sohler, D. B. Ostrowsky, O. Alibart, and S. Tanzilli. A polarization entangled photon-pair source based on a type-ii ppln waveguide emitting at a telecom wavelength. *New Journal of Physics*, 12(10):103005, 2010.
- [26] M. Fiorentino, S. M. Spillane, R. G. Beausoleil, T. D. Roberts, P. Battle, and M. W. Munro. Spontaneous parametric down-conversion in periodically poled ktp waveguides and bulk crystals. *Opt. Express*, 15(12):7479–7488, Jun 2007.
- [27] R. Regener and W. Sohler. Loss in low-finesse ti:linbo3 optical waveguide resonators. *Applied Physics B: Lasers and Optics*, 36:143–147, 1985.
- [28] H. J. Kimble, M. Dagenais, and L. Mandel. Photon antibunching in resonance fluorescence. *Phys. Rev. Lett.*, 39:691–695, Sep 1977.
- [29] P. Grangier, G. Roger, and A. Aspect. Experimental evidence for a photon anticorrelation effect on a beam splitter: A new light on single-photon interferences. *EPL (Europhysics Letters)*,

- 1(4):173, 1986.
- [30] J. F. Clauser. Experimental distinction between the quantum and classical field-theoretic predictions for the photoelectric effect. *Phys. Rev. D*, 9:853–860, Feb 1974.
  - [31] R. Q. Hanbury Brown, R. and Twiss. Correlation between photons in two coherent beams of light. *Nature*, 177:27–29, 1956.
  - [32] A. B. U'Ren, C. Silberhorn, J. L. Ball, K. Banaszek, and I. A. Walmsley. Characterization of the nonclassical nature of conditionally prepared single photons. *Phys. Rev. A*, 72:021802, Aug 2005.
  - [33] S. Fasel, O. Alibart, S. Tanzilli, P. Baldi, A. Beveratos, A. Gisin, and H. Zbinden. High-quality asynchronous heralded single-photon source at telecom wavelength. *New Journal of Physics*, 6(1):163, 2004.
  - [34] D. N. Klyshko. Use of two-photon light for absolute calibration of photoelectric detectors. *Soviet Journal of Quantum Electronics*, 10(9):1112, 1980.
  - [35] R. J. Glauber. The quantum theory of optical coherence. *Phys. Rev.*, 130:2529–2539, Jun 1963.
  - [36] S.-L. Tsao and C.-Y. Lu. Bpm simulation and comparison of 1x2 directional waveguide coupling and y-junction coupling silicon-on-insulator optical couplers. *Fiber and Integrated Optics*, 21(6):417–433, 2002.
  - [37] E.A.J. Marcatili. Dielectric rectangular waveguide and directional coupler for integrated optics. *Bell System Technical Journal*, 48:2071–2102, 1969.
  - [38] W. K. Burns, A. F. Milton, A. B. Lee, and E. J. West. Optical modal evolution 3-db coupler. *Appl. Opt.*, 15(4):1053–1065, Apr 1976.
  - [39] L. Bersiner, U. Hempelmann, and E. Strake. Numerical analysis of passive integrated-optical polarization splitters: comparison of finite-element method and beam-propagation method results. *J. Opt. Soc. Am. B*, 8(2):422–433, Feb 1991.
  - [40] E. Strake, G.P. Bava, and I. Montrosset. Guided modes of ti:linbo3 channel waveguides: a novel quasi-analytical technique in comparison with the scalar finite-element method. *Lightwave Technology, Journal of*, 6(6):1126–1135, jun 1988.
  - [41] M. Yamada, N. Nada, M. Saitoh, and K. Watanabe. First-order quasi-phase matched LiNbO3 waveguide periodically poled by applying an external field for efficient blue second-harmonic generation. *Applied Physics Letters*, 62(5):435–436, February 1993.
  - [42] Y. Zhang, Z. D. Gao, Z. Qi, S. N. Zhu, and N. B. Ming. Nonlinear cerenkov radiation in nonlinear photonic crystal waveguides. *Phys. Rev. Lett.*, 100:163904, Apr 2008.
  - [43] P. J. Mosley, J. S. Lundeen, B. J. Smith, P. Wasylczyk, A. B. U'Ren, C. Silberhorn, and I. A. Walmsley. Heralded generation of ultrafast single photons in pure quantum states. *Phys. Rev. Lett.*, 100:133601, Apr 2008.
  - [44] C. Söller, O. Cohen, B. J. Smith, I. A. Walmsley, and C. Silberhorn. High-performance single-photon generation with commercial-grade optical fiber. *Phys. Rev. A*, 83:031806, Mar 2011.
  - [45] F. Steinlechner, P. Trojek, M. Jofre, H. Weier, D. Perez, T. Jennewein, R. Ursin, J. Rarity, M. W. Mitchell, J. P. Torres, H. Weinfurter, and V. Pruneri. A high-brightness source of polarization-entangled photons optimized for applications in free space. *Opt. Express*, 20(9):9640–9649, Apr 2012.